Lukas Heletta, Theresa Block, Steffen Klenner and Rainer Pöttgen\*

# Ternary transition metal gallides with TiNiSi, ZrBeSi and MgZn<sub>2</sub>-type structure

https://doi.org/10.1515/znb-2019-0002 Received January 4, 2019; accepted January 11, 2019

Abstract: A series of ternary transition metal gallides around the equiatomic composition have been synthesized from the elements by arc-melting and subsequent annealing. The compounds crystallize with site occupancy variants of the hexagonal Laves phase MgZn<sub>2</sub>, with the hexagonal ZrBeSi or the orthorhombic TiNiSi type. All samples have been characterized on the basis of their lattice parameters, determined by X-ray powder diffraction (Guinier technique). The structures of NbCr<sub>158</sub>Ga<sub>0.62</sub> and NbFe<sub>151</sub>Ga<sub>0.49</sub> (MgZn<sub>2</sub> type, P6<sub>3</sub>/mmc), NbRhGa (ZrBeSi type, P6,/mmc), and ScNiGa, ScPtGa and ScAuGa (TiNiSi type, *Pnma*) were refined from single crystal X-ray diffractometer data. The ScPtGa and ScAuGa crystals showed trilling formation. Mixed site occupancies were only observed in the Laves phases while all other crystals were well ordered. A striking structural motif of NbRhGa is the formation of niobium chains (264 pm Nb-Nb) along the c axis. Several gallides were magnetically characterized. They are Pauli paramagnets. The two crystallographically independent iron sites in the Laves phase TaFeGa could be distinguished in the <sup>57</sup>Fe Mössbauer spectrum. The isomer shifts of 0.06(3) (Fe1) and -0.02(3) (Fe2) mm s<sup>-1</sup> indicate metallic iron.

**Keywords:** crystal structure; <sup>57</sup>Fe Mössbauer spectroscopy; gallides; Laves phase.

#### 1 Introduction

Of the three Laves phase types [1–3] those with the cubic  $MgCu_2$  and the hexagonal  $MgZn_2$  type have mainly binary and ternary representatives [4]. The formation of one of these types depends on the valence electron count (VEC).

\*Corresponding author: Rainer Pöttgen, Institut für Anorganische und Analytische Chemie, Universität Münster, Corrensstrasse 30, 48149 Münster, Germany, e-mail: pottgen@uni-muenster.de Lukas Heletta, Theresa Block and Steffen Klenner: Institut für Anorganische und Analytische Chemie, Universität Münster, Corrensstrasse 30, 48149 Münster, Germany

Various studies of Laves phase solid solutions along with detailed electronic structure calculations confirmed these trends [5–11].

Besides the statistical site occupancies within the solid solutions, the two Laves phase types allow ordering variants. The simplest possibility occurs for the MgZn type. In the silicide Mg<sub>2</sub>Cu<sub>2</sub>Si [12], coloring of the 2a and 6h sites with silicon, respectively copper atoms leads to superstructure formation without the need for symmetry reduction. This is the key difference with respect to all other Laves phase superstructures. Similar compositions occur for the silicide Mg<sub>2</sub>Ni<sub>2</sub>Si [13] and the series of RE<sub>2</sub>Rh<sub>2</sub>Ga (RE=Y, La-Nd, Sm, Gd-Er) gallides [14]; however, these phases are derived from the cubic Laves phase MgCu, and require a rhombohedral distortion in order to enable the 3:1 ordering on the tetrahedral network. A 7:1 ordering variant has been reported for Cd<sub>2</sub>Cu<sub>2</sub>As [15]. Ordering is also possible on the magnesium site. MgCu, shows the MgSnCu [16, 17] superstructure variant which is possible in the non-centrosymmetric subgroup  $F\overline{4}3m$ , splitting the 8b site into two fourfold sites.

The Pearson data base lists a large number of equiatomic phases for which the  ${\rm MgZn_2}$  structure has been assigned. This is only possible with mixed-occupied sites. During recent studies on the equiatomic gallides *RE*IrGa we observed the phases  $RE_6{\rm Ir_5Ga_7}$  ( $RE={\rm Sc}$ , Y, Nd, Sm, Gd-Lu) [18, 19] which are very close in composition, i.e.  $RE{\rm Ir_{0.83}Ga_{1.17}}$ . Motivated by this new ordering variant we started a more systematic study of ternary transition metal gallides around the equiatomic composition. Herein we report on the synthesis, structure refinements and some physical properties of such hexagonal Laves phases and the equiatomic gallides ScNiGa, ScPtGa, ScAuGa, and NbRhGa which crystallize with different AlB<sub>2</sub> superstructures.

# 2 Experimental

## 2.1 Synthesis

The ternary gallides listed in Tables 1 and 2 were synthesized directly from the elements by arc-melting. The transition metals (*T*) were used as ingots, powders, chips,

Table 1: Refined lattice parameters (Guinier powder data) of several transition metal gallides with the MgZn, Laves phase structure (with transition metal gallium mixing), space group P6<sub>3</sub>/mmc.

Composition	a (pm)	<i>c</i> (pm)	V (nm³)	Reference
ScMnGa	518.2(2)	849.6(3)	0.1976	This work
$ScMn_{0.8}Ga_{1.2}$	522	852	0.2011	[22]
ScFeGa	504.8(2)	824.0(3)	0.1818	This work
ScFe <sub>1.37</sub> Ga <sub>0.63</sub>	505.3	828.7	0.1832	[22]
ScCoGa	513.8(2)	815.5(4)	0.1864	This work
ScCo <sub>1.13</sub> Ga <sub>0.87</sub>	502.1	813.7	0.1777	[23]
ScNi <sub>1.31</sub> Ga <sub>0.69</sub>	505.4	800.2	0.1770	[23]
ScRuGaª	522.2(2)	841.1(2)	0.1986	This work
ScRhGa	911.6(2)	822.8(1)	0.5922	This work
ScIrGaª	913.6(3)	818.5(2)	0.5916	This work
ScIrGa⁵	913.79(4)	817.67(4)	0.5913	This work
Sc <sub>6</sub> Ir <sub>5</sub> Ga <sub>7</sub>	911.8(2)	828.0(1)	0.5962	[19]
ZrCoGaª	510.3(3)	819.3(4)	0.1848	This work
NbCrGa	499.3(1)	822.4(2)	0.1776	This work
NbCrGa	497.2	822.8	0.1762	[24]
$NbCr_{1.5}Ga_{0.5}$	494.5(2)	822.4(3)	0.1742	This work
NbMnGa	499.4(1)	814.5(2)	0.1759	This work
$NbMn_{\scriptscriptstyle{1.5}}Ga_{\scriptscriptstyle{0.5}}$	495.3(3)	807.6(4)	0.1716	This work
$Nb_{0.9}Mn_{1.8}Ga_{0.3}$	491.7	800.2	0.1675	[25]
NbFeGaª	496.9(2)	807.7(2)	0.1727	This work
$NbFe_{\scriptscriptstyle{1.5}}Ga_{\scriptscriptstyle{0.5}}$	490.3(2)	799.3(3)	0.1664	This work
NbCoGa <sup>a</sup>	495.2(1)	797.9(2)	0.1694	This work
$NbCo_{\scriptscriptstyle{1.5}}Ga_{\scriptscriptstyle{0.5}}$	487.0(3)	789.2(3)	0.1621	This work
$NbCo_{\scriptscriptstyle{1.5}}Ga_{\scriptscriptstyle{0.5}}$	487.0	789.3	0.1621	[26]
NbNiGa	494.8(1)	793.8(1)	0.1683	This work
$NbNi_{1.5}Ga_{0.5}$	488.5(2)	791.7(3)	0.1636	This work
$NbNi_{1.5}Ga_{0.5}$	488.2	788.5	0.1628	[26]
NbCuGa	501.3(3)	807.2(5)	0.1757	[27, 28]
TaCrGa	496.3(2)	821.3(3)	0.1752	This work
$TaCr_{1.5}Ga_{0.5}$	496.7(1)	815.1(2)	0.1742	This work
TaMnGa <sup>a</sup>	497.6(1)	811.8(2)	0.1741	This work
$TaMn_{\scriptscriptstyle{1.5}}Ga_{\scriptscriptstyle{0.5}}$	496.6(1)	808.1(2)	0.1726	This work
TaFeGa	494.5(3)	804.0(3)	0.1703	This work
$TaFe_{1.5}Ga_{0.5}$	488.7(1)	795.6(2)	0.1646	This work
TaCoGa	493.0(3)	795.0(5)	0.1673	This work
$TaCo_{1.5}Ga_{0.5}$	486.1(1)	786.9(2)	0.1610	This work
$TaCo_{1.5}Ga_{0.5}$	486.0	786.1	0.1608	[26]
TaNiGa	493.7(2)	794.1(2)	0.1676	This work
TaNi <sub>1.5</sub> Ga <sub>0.5</sub>	487.3(3)	789.9(4)	0.1624	This work
TaNi <sub>1.5</sub> Ga <sub>0.5</sub>	487.2	787.3	0.1618	[26]

<sup>a</sup>These samples were not annealed; <sup>b</sup>single crystal data. Note that the ScRhGa and ScIrGa samples adopt a  $\sqrt{3}a \times \sqrt{3}a \times c$  superstructure variant, space group P63/mcm (Yb61r6Ga7 type with small degrees of Rh/Ga respectively Ir/Ga mixing). Standard deviations are given in parentheses.

granules or sponge from different suppliers, all with stated purities better than 99.9%. The gallium pieces (Smart Elements) had a metal-based purity of 99.999%.

The elements were mixed in the ideal T:T':X=1:1:1 or 2:3:1 atomic ratios (the powders were cold-pressed to pellets) and were arc-melted under an argon pressure of 700-800 mbar using a home-made water-cooled copper crucible [20]. The argon (Westfalen, 99.998%) was purified over titanium sponge (T=900 K), silica gel, and molecular sieves. The product ingots were turned over and re-melted several times to ensure sample homogeneity. The weight losses after the repeated arc-melting were always smaller than 1%. Most buttons were subsequently sealed in evacuated silica tubes and annealed at T=1073 K for 30 days. At the end of the annealing sequence the samples were quenched in ice water. The polycrystalline samples are all air-stable and show the typical metallic lustre.

## 2.2 X-ray image plate data and data collection

The gallide samples were characterized by powder X-ray diffraction after the arc-melting as well as after the annealing sequence using a Guinier camera (Enraf-Nonius FR552 equipped with a Fuji-film image plate system, BAS-1800) equipped with  $CuK\alpha_1$  radiation and  $\alpha$ -quartz (a=491.30, c=540.46 pm) as an internal standard. The lattice parameters (Tables 1 and 2) were obtained from standard least-squares refinements from the powder data. The experimental patterns were compared to calculated ones to ensure proper indexing [21]. Our data agree with previous literature reports [22–31]. The discrepancies for ScPtGa are discussed in the crystal chemical section.

Crystal fragments were selected from several of the crushed annealed Laves phase samples as well as from the crushed ingots of ScNiGa, ScPtGa, ScAuGa and NbRhGa. The crystals were glued to quartz fibers using bees wax and their quality for intensity data collection was first checked by Laue photographs on a Buerger camera (white Mo radiation, image plate technique, Fuji-film, BAS-1800). Data sets were collected either on a Stoe StadiVari diffractometer equipped with a Mo micro focus source and a Pilatus detection system or on a Stoe IPDS-II two-circle diffractometer with graphitemonochromatized Mo radiation ( $\lambda = 71.073$  pm). Due to a Gaussian-shaped profile of the micro focus source, scaling was applied along with the numerical absorption correction. All relevant crystallographic data and details of the data collections and evaluations are listed in Tables 3 and 4.

Table 2: Refined lattice parameters (Guinier powder data) of several equiatomic transition metal gallides.

Compound	Туре	Space group	a (pm)	<i>b</i> (pm)	<i>c</i> (pm)	V (nm³)	Reference
ScNiGa	TiNiSi	Pnma	631.2(1)	416.0(1)	722.8(2)	0.1898	This work
ScNiGa	KHg,	Imma	416.4(1)	630.6(1)	723.0(1)	0.1899	[29]
ScCu <sub>0.95</sub> Ga <sub>1.05</sub>	KHg,	Imma	422.9	645.0	732.5	0.1998	[30]
ScPdGa	TiNiSi	Pnma	628.1(7)	435.82(7)	755.20(5)	0.2067	[31]
ScPtGa	TiNiSi	Pnma	630.8(2)	433.4(1)	751.4(1)	0.2054	This work
ScPtGa	TiNiSi	Pnma	645.4(2)	434.2(1)	747.9(3)	0.2096	[31]
ScAuGa	TiNiSi	Pnma	659.4(2)	436.40(8)	756.3(2)	0.2176	This work
NbRhGa	ZrBeSi	P6 <sub>3</sub> /mmc	444.2(6)	а	530.6(7)	0.0907	This work

Standard deviations are given in parentheses.

**Table 3:** Single crystal data and structure refinements for ScTGa (T = Ni, Pt, Au) and NbRhGa.

Empirical formula	ScNiGa	ScPtGa	ScAuGa	NbRhGa
Formula weight, g mol <sup>-1</sup>	173.4	309.8	311.6	265.5
Lattice parameters (single crystal	data)			
a, pm	631.20(1)	629.88(5)	660.92(4)	444.63(8)
<i>b</i> , pm	416.00(1)	433.35(4)	435.21(7)	а
<i>c</i> , pm	722.8(2)	751.81(6)	753.56(6)	527.38(9)
Cell volume, nm³	0.1898	0.2052	0.2168	0.0903
Space group	Pnma	Pnma	Pnma	P6 <sub>3</sub> /mmc
Formula units, Z	4	4	4	2
Calculated density, g cm <sup>-3</sup>	6.07	10.03	9.55	9.77
Crystal size, $\mu$ m <sup>3</sup>	$20 \times 30 \times 50$	$40 \times 60 \times 75$	$20 \times 30 \times 40$	$30\times40\times40$
Diffractometer	IPDS II	IPDS II	StadiVari	IPDS II
Radiation	Mo $Κα$	Mo $K$ $α$	Mo $Κα$	Mο $K\alpha$
Transmission min/max	0.459/0.721	0.084/0.118	0.047/0.159	0.404/0.420
Detector distance, mm	70	70	40	70
Exposure time, s	360	300	30	240
Integr. Param. A/B/EMS	12.7/2.9/0.012	12.0/3.0/0.02	6.5/-4.0/0.02	14.0/-1.0/0.03
Abs. coefficient, mm <sup>-1</sup>	26.8	83.7	83.4	29.5
F(000), e	320	520	524	234
$\theta$ range, deg	4.3-33.3	4.2-33.3	4.1-33.5	5.3-33.2
hkl range	$\pm 9, \pm 6, \pm 11$	$\pm 9, \pm 6, \pm 11$	$\pm 10, \pm 6, \pm 11$	$\pm 6, \pm 6, \pm 8$
Total no. reflections	9313	5603	9705	1461
Independent reflections, $R_{int}$	398/0.0599	631/0.0892	668/0.0642	85/0.0209
Refl. with $I \ge 3 \sigma(I)$ , $R_{\sigma}$	344/0.0132	536/0.0108	527/0.0133	64/0.0044
Data/parameters	398/20	631/22	668/22	85/8
Goodness-of-fit on F <sup>2</sup>	1.84	1.71	1.63	2.17
$R_1/wR_2$ for $I \ge 3 \sigma(I)$	0.0267/0.0566	0.0235/0.0499	0.0229/0.0574	0.0141/0.0629
$R_1/wR_2$ for all data	0.0352/0.0580	0.0292/0.0509	0.0311/0.0580	0.0228/0.0638
Trilling ratio, %	_	60.6(5):5.2:34.2	37.4(13):26.9:35.7	_
Extinction coefficient	2600(500)	440(50)	40(5)	81(17)
Largest diff. peak/hole, e Å-3	1.56/-1.20	2.32/-2.56	2.68/-1.93	2.50/-1.67

#### 2.3 EDX data

The six single crystals studied on the diffractometers were semi-quantitatively analysed by EDX using a Zeiss EVO® MA10 scanning electron microscope which was operated in variable pressure mode (60 Pa). Sc, Nb, Cr, Fe, Ni, Rh, Pt, Au, and GaP were used as internal standards. Several points on each crystal were analysed with a

Table 4: Single crystal data and structure refinements of the hexagonal Laves phases  $NbCr_{1.58}Ga_{0.42}$  and  $NbFe_{1.51}Ga_{0.49}$  at room temperature.

Empirical formula	NbCr <sub>1.58(1)</sub> Ga <sub>0.42(1)</sub>	NbFe <sub>1.51(1)</sub> Ga <sub>0.49(1)</sub>		
Formula weight, g mol <sup>-1</sup>	204.4	211.3		
Lattice parameters (single crys	tal data)			
<i>a</i> , pm	494.63(9)	490.60(4)		
<i>c</i> , pm	822.4(1)	799.46(6)		
Cell volume, nm³	0.1742	0.1666		
Space group	P6 <sub>3</sub> /mmc	P6 <sub>3</sub> /mmc		
Formula units, Z	4	4		
Calculated density, g cm <sup>-3</sup>	7.79	8.42		
Crystal size, $\mu$ m <sup>3</sup>	$20\!\times\!20\!\times\!20$	$60 \times 40 \times 20$		
Diffractometer	StadiVari	IPDS II		
Radiation	Mo $K$ $α$	Mo $Kα$		
Transmission min/max	0.528/0.537	0.385/0.613		
Detector distance, mm	40	70		
Exposure time, s	20	600		
Integr. Param. A/B/EMS	7.0/-6.0/0.03	13.0/3.0/0.014		
Abs. coefficient, mm <sup>-1</sup>	22.0	26.9		
F(000), e	368	382		
$\theta$ range, deg	4.8-31.8	4.8-33.4		
hkl range	$\pm 7, \pm 7, \pm 13$	$\pm 7, \pm 7, \pm 12$		
Total no. reflections	1736	4078		
Independent reflections, $R_{int}$	140/0.0220	152/0.0535		
Refl. with $l \ge 3 \sigma(l)$ , $R_{\sigma}$	123/0.0073	130/0.0048		
Data/parameters	140/13	152/13		
Goodness-of-fit on F <sup>2</sup>	0.77	1.16		
$R_1/wR_2$ for $I \ge 3 \sigma(I)$	0.0088/0.0204	0.0113/0.0285		
$R_1/wR_2$ for all data	0.0112/0.0213	0.0183/0.0300		
Extinction coefficient	109(13)	1690(130)		
Largest diff. peak/hole, <i>e</i> Å <sup>-3</sup>	0.30/-0.32	0.92/-0.90		

secondary electron detector. The experimentally observed compositions matched the ones obtained from the singe crystal X-ray data within ±3 at-%. The standard deviation accounts for the irregular crystal surfaces (conchoidal fracture). No impurity elements were detected.

#### 2.4 Physical property measurements

The magnetic properties of the gallide samples which were pure on the level of X-ray powder diffraction were measured with the VSM option of a Physical Property Measurement System (QuantumDesign PPMS-9). The susceptibilities were measured with an applied magnetic field of 10 kOe  $(1 \text{ kOe} = 7.96 \times 10^4 \text{ A m}^{-1})$  in the temperature range of 3–300 K.

#### 2.5 Mössbauer spectroscopy

The TaFeGa sample was further characterized through its room-temperature <sup>57</sup>Fe Mössbauer spectrum using a <sup>57</sup>Co/Rh source. The sample was placed in a thin walled PMMA

container with an optimized thickness according to Long et al. [32]. The measurement was conducted in usual transmission geometry with a counting time of 1 day. The WIN-NORMOS for IGOR6 routine [33] was used for fitting the spectrum.

#### 3 Results and discussion

#### 3.1 Structure refinements

The NbCr<sub>1.58</sub>Ga<sub>0.42</sub> and NbFe<sub>1.51</sub>Ga<sub>0.49</sub> data sets show hexagonal lattices with high Laue symmetry, and the systematic extinctions were compatible with space group P6,/mmc. The starting atomic parameters were determined with the charge-flip algorithm [34] of SUPERFLIP [35] and the two structures were refined on  $F^2$  with the JANA2006 [36] software package using anisotropic displacement parameters for all atoms. Refinements of the occupancy parameters revealed mixed occupancy for the 2a and 6h sites of both crystals. These occupancies were included as leastsquares parameters in the final cycles.

The NbRhGa crystal also showed a hexagonal lattice with high Laue symmetry. The systematic extinctions were compatible with space group P6/mmc; however, the powder pattern already pointed to an AlB, superstructure. The structure refinement confirmed the ZrBeSi type [37] and all sites were fully occupied within two standard deviations.

The situation is more complex for the equiatomic gallides ScNiGa, ScPtGa and ScAuGa. The Guinier patterns pointed to isotypism with the orthorhombic TiNiSi-type structure [38], space group *Pnma*. For ScNiGa the structure refinement was straightforward, confirming the fully ordered TiNiSi type, which is an orthorhombically distorted superstructure of the aristotype AlB, [39, 40]. The symmetry reduction proceeds via three steps of which the first one is the translationengleiche t3 transition to the orthohexagonal setting in space group Cmmm. This t3 transition can induce trilling formation, especially for those orthorhombic cells which have c/b ratios close to  $\sqrt{3}$ (≈1.7321). This is the case for the ScPtGa (c/b = 1.735) and ScAuGa (c/b = 1.731) crystals and the trilling refinements were conducted with the following matrices:

$$M_{2} = \begin{pmatrix} 1 & 0 & 0 \\ 0 & -\frac{1}{2} & \frac{1}{2} \\ 0 & -\frac{3}{2} & -\frac{1}{2} \end{pmatrix}; \quad M_{3} = \begin{pmatrix} 1 & 0 & 0 \\ 0 & -\frac{1}{2} & -\frac{1}{2} \\ 0 & \frac{3}{2} & -\frac{1}{2} \end{pmatrix}$$

Table 5: Atomic coordinates and isotropic displacement parameters (pm²) of the studied transition metal gallides.

Atom	Wyckoff position	х	у	Z	$U_{\rm eq}$
ScNiGa					
Sc	4 <i>c</i>	0.01221(14)	1/4	0.70196(13)	103(2)
Ni	4 <i>c</i>	0.27573(11)	1/4	0.40361(9)	111(2)
Ga	4 <i>c</i>	0.18360(9)	1/4	0.07593(7)	107(2)
ScPtGa					
Sc	4 <i>c</i>	0.0089(4)	1/4	0.7116(3)	162(5)
Pt	4 <i>c</i>	0.26635(7)	1/4	0.40840(6)	153(1)
Ga	4 <i>c</i>	0.19150(17)	1/4	0.07915(17)	174(3)
ScAuGa					
Sc	4 <i>c</i>	0.0021(5)	1/4	0.7199(4)	209(6)
Au	4 <i>c</i>	0.27975(10)	1/4	0.4161(2)	214(2)
Ga	4 <i>c</i>	0.20852(16)	1/4	0.0852(5)	225(5)
NbRhGa					
Nb	2 <i>a</i>	0	0	0	51(4)
Rh	2 <i>c</i>	1/3	2/3	1/4	59(3)
Ga	2 <i>d</i>	1/3	2/3	3/4	62(4)
NbCr <sub>1.58</sub> Ga <sub>0.42</sub>					
Nb 1.35 0.42	4 <i>f</i>	1/3	2/3	0.56328(3)	131(1)
0.41(1) Cr1/0.59(1) Ga1	2 <i>a</i>	0	0	0	135(2)
0.91(1) Cr2/0.09(1) Ga2	6 <i>h</i>	0.17196(5)	2 <i>x</i>	1/4	138(1)
$NbFe_{1.51}Ga_{0.49}$					
Nb	4 <i>f</i>	1/3	2/3	0.56273(4)	57(1)
0.68(1) Fe1/0.32(1) Ga1	2 <i>a</i>	0	0	0	62(2)
0.78(1) Fe2/0.22(1) Ga2	6h	0.17025(6)	2 <i>x</i>	1/4	61(2)

The isotropic displacement parameter  $U_{eq}$  is defined as  $U_{eq} = 1/3$  ( $U_{11} + U_{22} + U_{33}$ ). Standard deviations are given in parentheses.

The resulting domain ratios are listed in Table 3. Refinements of the occupancy parameters in separate least-squares cycles revealed full occupancy within two standard deviations for the three scandium compounds. The final difference Fourier analyses revealed no significant residual electron densities. All positional and displacement parameters and interatomic distances are listed in Tables 5-7.

CCDC 1888747 (NbCr<sub>1.58</sub>Ga<sub>0.42</sub>), 1888749 (NbFe<sub>1.51</sub>Ga<sub>0.49</sub>), 1888746 (ScNiGa), 1888743 (ScPtGa), 1888741 (ScAuGa) and 1888742 (NbRhGa) contain the supplementary crystallographic data for this paper. These data can be obtained free of charge from The Cambridge Crystallographic Data Centre via www.ccdc.cam.ac.uk/data\_request/cif.

# 3.2 Crystal chemistry

We start the crystal chemical description with the hexagonal Laves phases. Synthesis of several samples with both the 1:1:1 and 1:1.5:0.5 (≡2:3:1) compositions showed the formation of extended solid solutions with transition metal/ gallium mixing on the 2a and 6h sites of the tetrahedral network. The differences in the *a* and *c* lattice parameters of the 1:1:1 and 1:1.5:0.5 compositions account for the transition metal/gallium mixing.

Table 6: Interatomic distances (pm) in the structures of  $NbCr_{1.58}Ga_{0.42}$  and  $NbFe_{1.51}Ga_{0.49}$ .

NbCr <sub>1.58</sub> Ga	0.42			NbFe <sub>1.51</sub> Ga	0.49		
Nb:	3	Ga1/Cr1	290.3	Nb:	3	Ga2/Fe2	285.9
	6	Ga2/Cr2	291.1		6	Ga2/Fe2	287.4
	3	Ga2/Cr2	292.4		3	Ga1/Fe1	287.7
	3	Nb	304.0		1	Nb	299.4
	1	Nb	307.1		3	Nb	300.5
Ga1/Cr1:	6	Ga2/Cr2	252.9	Ga1/Fe1:	6	Ga2/Fe2	246.7
	6	Nb	290.3		6	Nb	287.7
Ga2/Cr2:	2	Ga2/Cr2	239.5	Ga2/Fe2:	2	Ga2/Fe2	240.0
	2	Ga1/Cr1	252.9		2	Ga1/Fe1	246.7
	2	Ga2/Cr2	255.2		2	Ga2/Fe2	250.6
	4	Nb	291.1		2	Nb	285.9
	2	Nb	292.4		4	Nb	287.4

All distances within the first coordination spheres are listed. Standard deviations are all equal or smaller than 0.1 pm.

The situation is different for the scandium compounds ScRhGa and ScIrGa. The Guinier powder patterns of both samples already showed superstructure reflections after the arc-melting, pointing to Rh/Ga respectively Ir/Ga ordering of the Yb, Ir, Ga, type [18], also observed for Sc<sub>2</sub>Ir<sub>5</sub>Ga<sub>7</sub> [19]. While the ScRhGa sample was microcrystalline also after several annealing steps, the ScIrGa sample allowed for a selection of small single crystals.

**Table 7:** Interatomic distances (pm) in the structures of ScTGa (T = Ni, Pt, Au) and NbRhGa.

ScNi	Ga			ScPt	Sa			ScAu	Ga			NbRh	Ga		
Sc:	1	Ni	272.3	Sc:	1	Pt	279.7	Sc:	1	Au	293.4	Nb:	2	Nb	263.7
	2	Ni	286.6		2	Pt	291.8		2	Ga	297.2		6	Rh	288.6
	2	Ni	287.1		2	Ga	296.0		2	Au	300.0		6	Ga	288.6
	1	Ga	288.7		1	Ga	296.2		1	Ga	300.8				
	2	Ga	290.4		2	Pt	298.1		2	Au	304.2				
	1	Ga	291.1		1	Ga	299.3		2	Ga	307.0				
	2	Ga	297.4		2	Ga	304.1		1	Ga	307.2				
	1	Ni	321.8		2	Sc	320.2		1	Au	311.2				
	2	Sc	323.2		1	Pt	324.0		2	Sc	333.6				
	2	Sc	358.8		2	Sc	385.1		2	Sc	396.5				
Ni:	2	Ga	243.8	Pt:	1	Ga	252.0	Au:	2	Ga	252.3	Rh:	3	Ga	256.7
	1	Ga	243.9		2	Ga	253.2		1	Ga	253.8		2	Ga	263.7
	1	Ga	257.9		1	Ga	268.0		1	Ga	283.4		6	Nb	288.6
	1	Sc	272.3		1	Sc	279.7		1	Sc	293.4				
	2	Sc	286.6		2	Sc	291.8		2	Sc	300.0				
	2	Sc	287.1		2	Sc	298.1		2	Sc	304.2				
	1	Sc	321.8		1	Sc	324.0		1	Sc	311.2				
Ga:	2	Ni	243.8	Ga:	1	Pt	252.0	Ga:	2	Au	252.3	Ga:	3	Rh	256.7
	1	Ni	243.9		2	Pt	253.2		1	Au	253.8		2	Rh	263.7
	1	Ni	257.9		1	Pt	268.0		1	Au	283.4		6	Nb	288.6
	1	Sc	288.7		2	Sc	296.0		2	Sc	297.2				
	2	Sc	290.4		1	Sc	296.2		1	Sc	300.8				
	1	Sc	291.1		1	Sc	299.3		2	Sc	307.0				
	2	Sc	297.4		2	Sc	304.1		1	Sc	307.2				

All distances within the first coordination spheres are listed. Standard deviations are all equal or smaller than 0.1 pm.

Although the data set was of bad quality (and not documented herein), refinement with the structural model of the  $Yb_sIr_sGa_7$  type led to a composition  $Sc_6Ir_{5.99}Ga_{6.01}$  (close to the starting composition) with 76/24(1)% Ir/Ga mixing on the 12j and 20/80(1)% Ir/Ga mixing on the 4d Wyckoff sites. We can thus assume solid solutions Sc. Rh, Ga,++, Ga,++ and Sc<sub>6</sub>Ir<sub>5+v</sub>Ga<sub>7+v</sub> around the equiatomic compositions.

As an example we present the Guinier powder pattern of the ScRhGa sample in Fig. 1. The strongest superstructure reflections for the  $\sqrt{3} \times \sqrt{3} \times c$  cell are marked in red. Those marked in blue color correspond to a primitive cubic cell with a lattice parameter of 314 pm which is in between the binaries RhGa (300.6 pm) [41] and ScRh (320.6 pm) [42], indicating a solid solution of the three elements on a CsCl cell with some long-range order; thus the primitive reflections. At first sight one might think that the small byproduct could be the Heusler phase ScRh, Ga [43]; however its lattice parameter is 619.2 ( $\equiv$ 2×309.6 pm) and this is too small with respect to the present phase.

Figure 2 shows a projection of the NbCr<sub>1.58</sub>Ga<sub>0.42</sub> and Sc<sub>6</sub>Ir<sub>5 99</sub>Ga<sub>6 01</sub> structures along the hexagonal axes. Both structures show transition metal/gallium mixing onto the tetrahedral networks; however, with different consequences. To a first approximation, the hexagonal Laves phase structures

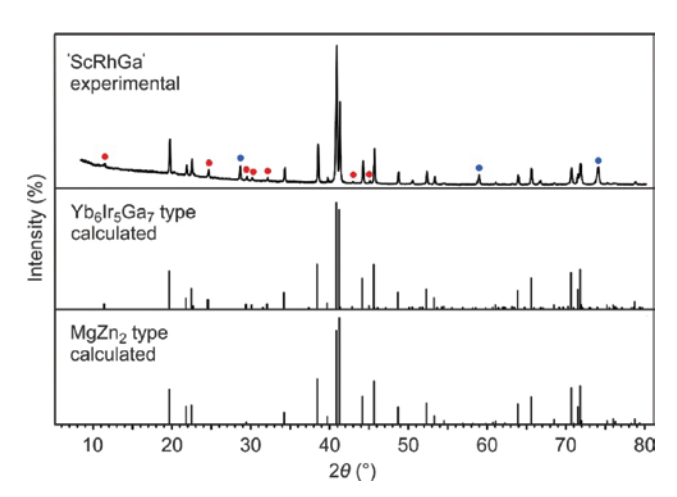


Fig. 1: Guinier powder pattern of the ScRhGa sample (top) along with calculated patterns assuming the ordered Yb, Ir, Ga, type (middle) and the MgZn, subcell with Ir/Ga statistics (bottom). The red dots mark the strongest superstructure reflections, manifesting the Ir/Ga ordering of the Ybs Irs Gaz type. Blue circles correspond to a small by-product of a cubic CsCl-type phase with a lattice parameter of 314 pm which is in between the binaries RhGa (300.6 pm) [41] and ScRh (320.6 pm) [42].

can be described as hexagonal rod packings of cornerand face-sharing tetrahedra with shorter distances within than between the tetrahedra. The rows in the NbCr<sub>158</sub>Ga<sub>0/2</sub>

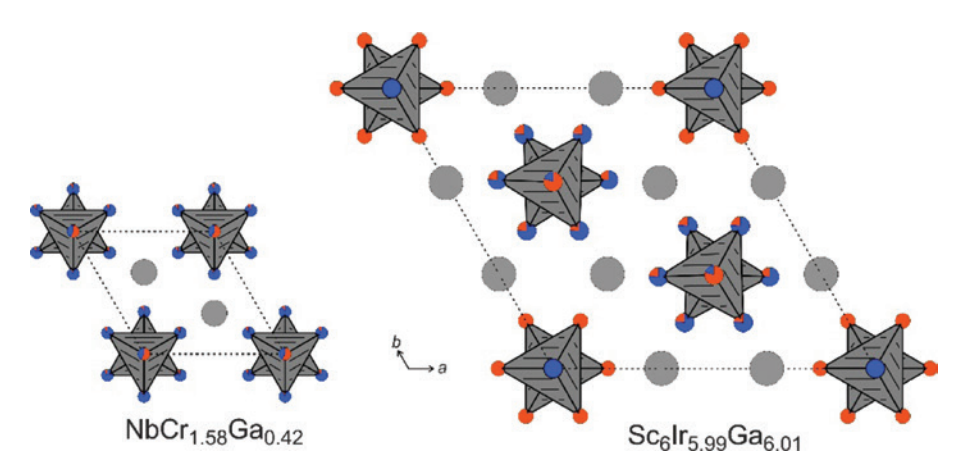


Fig. 2: Projection of the NbCr<sub>1.58</sub>Ga<sub>0.42</sub> (left) and Sc<sub>6</sub>Ir<sub>5.99</sub>Ga<sub>6.61</sub> (right) structures along the hexagonal axes. Niobium (scandium), chromium (iridium) and gallium atoms are drawn as medium grey, blue and red circles, respectively. The rows of edge- and corner-sharing tetrahedra are emphasized. NbCr<sub>1.58</sub>Ga<sub>0.62</sub> adopts the MgZn<sub>2</sub> subcell structure, and Sc<sub>6</sub>Ir<sub>5.99</sub>Ga<sub>6.01</sub> (~ScIrGa) crystallizes with the Yb<sub>6</sub>Ir<sub>5</sub>Ga<sub>7</sub> [18] superstructure with some residual Ir/Ga disorder.

structure show Cr/Ga mixing on both sites, emphasized by blue and red segments. This is different for the  $Sc_6Ir_{599}Ga_{601}$ structure. The  $\sqrt{3}\times\sqrt{3}$  superstructure formation leads to a decoupling of the rows. Those extending along 0 0 z consist of fully ordered IrGa, tetrahedra, while those at 1/3 2/3 z and 2/3 1/3 z show Ir/Ga mixing on both Wyckoff sites. The complete ordering of one type of rows is the reason for superstructure formation (partial long-range order).

The order (Yb, Ir, Ga, type)/disorder (MgZn, type) in the ScIrGa sample plays mainly on the c lattice parameter (Table 1). From the description with the rod packing it is readily evident, that a substitution of the apices of the condensed tetrahedra with an element of different size changes the c parameter: 818.5 pm for the disordered ScIrGa and 828.0 pm for the ordered Sc<sub>2</sub>Ir<sub>2</sub>Ga<sub>2</sub> sample. This is similar to the observation of Hulliger for an off-stoichi*ometric* sample of composition ScIrGa with a *c* parameter of 816.25 pm [44].

Herein we have only discussed the relevant crystal chemical features that are relevant for understanding the gallides presented in this work. For the general crystal chemical details of Laves phases we refer to competent review articles ([5–11], and references cited therein).

Now we turn to the equiatomic phases ScNiGa, ScPtGa, ScAuGa, and NbRhGa and start with the niobium compound. The rhodium and gallium atoms build up planar Rh, Ga, hexagons with 257 pm Rh-Ga distances. The latter are only slightly longer than the sum of the covalent radii [45] for Rh + Ga of 250 pm and they compare well with the Rh-Ga distance of 260 pm in CsCltype RhGa [41]. Every other layer of planar Rh, Ga, hexagons is rotated by 60°, forcing the doubling of the AlB subcell in *c* direction (ZrBeSi-type structure, space group P6,/mmc [37]). This way we obtain a sandwich-like coordination for the niobium atoms by two Rh, Ga, hexagons (Fig. 3). The coordination sphere is completed by additional niobium atoms below and above the hexagons with Nb-Nb distances of 264 pm. This distance corresponds to half the lattice parameter c and is even shorter than the Nb-Nb distance of 285 pm in bcc niobium [46]. We can thus assume substantial Nb-Nb bonding along the c axis and this feature reminds of the NiAs-type intermetallics [1-3]. Each rhodium and gallium atom has trigonal prismatic niobium coordination. These Nb, prisms are severely compressed with 444 pm Nb-Nb within the triangular plane and 264 pm Nb-Nb for the rectangular edges, leading to strongly anisotropic Nb-Nb bonding. This structural behavior is similar to the isotyopic aluminides TiAuAl (291 and 441 pm Ti-Ti) [47] and TiPtAl (274 and 440 pm Ti-Ti) [48].

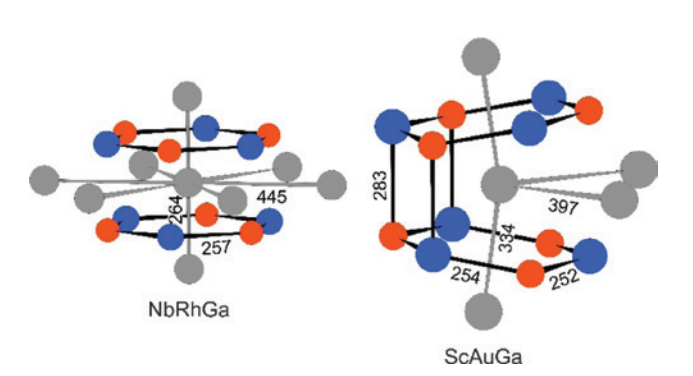


Fig. 3: Coordination polyhedra of the niobium and scandium atoms in NbRhGa (left) and ScAuGa (right). Niobium (scandium), rhodium (gold) and gallium atoms are drawn as medium grey, blue and red circles, respectively.

ScNiGa, ScPtGa and ScAuGa crystallize with the well-known TiNiSi-type structure, space group *Pnma*. The single crystal X-ray data clearly show the primitive reflections that manifest the transition metal/gallium ordering. ScAuGa is reported herein for the first time. Previous work on ScNiGa [30] and ScPtGa [31] was based only on powder X-ray data, and ScNiGa was ascribed to the KHg, type with Ni/Ga mixing. Since nickel and gallium differ by only three electrons, the weaker superstructure reflections have most likely been overlooked in the previous study. The lattice parameters reported by Dwight compare well with our data (Table 2) and most likely his older sample also had the correct composition and Ni/Ga ordering.

However, a distinct discrepancy occurs for ScPtGa. Our powder (Table 2) and single crystal (Table 3) lattice parameters show excellent agreement and the occupancy parameters (99.8(8)% for the platinum and 100.3(8)% for the gallium site) point to the ideal composition. The large deviations for the *a* and *c* parameters and the larger cell volume might indicate a different composition ScPt<sub>1+v</sub>Ga<sub>1+v</sub> for the sample studied by Hovestreydt et al. [31].

As an example we discuss the structure of ScAuGa. The gold and gallium atoms build up a three-dimensional polyanionic network with strongly distorted tetrahedral gallium coordination around gold and vice *versa*. The Au–Ga distances  $(2\times252, 1\times254 \text{ and } 1\times283)$ pm) underline this anisotropic bonding situation. The shorter ones indicate substantial covalent Au-Ga bonding. They are even shorter than the sum of the covalent radii [45] for Au+Ga of 259 pm. The shorter Au-Ga distances are within the tilted and slightly puckered Au<sub>3</sub>Ga<sub>3</sub> hexagons (Fig. 3), while the longer ones are interlayer Au-Ga bonds. Similar to NbRhGa discussed above, the scandium atoms in ScAuGa also have such a sandwich-like coordination; however, with orthorhombic distortion. The tilt of the hexagons leads to drastic changes in the Sc-Sc coordinations as compared to Nb-Nb. In ScAuGa we observe 2+2 scandium neighbors  $(2\times334 \text{ and } 2\times397 \text{ pm})$  as compared to the 2+6 Nb-Nb coordination in NbRhGa. The shorter Sc-Sc distances are comparable to those in hcp scandium ( $6 \times 325$  and 6×331 pm) [46], Sc<sub>3</sub>C<sub>4</sub> (314–367 pm) [49], Sc<sub>4</sub>Pt<sub>7</sub>Si<sub>2</sub> (305– 350 pm) [50] and the two modifications of ScPdGa (334-388 pm in LT-ScPdGa and 317-395 pm in HT-ScPdGa) [51]. For more crystal chemical details on the large family of TiNiSi-type intermetallics (>1600 entries in the Pearson data base [4]) we refer to review articles ([2, 39, 40, 52– 54], and references cited therein).

In parallel we studied the structures of ScCuGa and ScAgGa. They also crystallize with orthorhombically distorted superstructure variants of the aristotype AlB<sub>3</sub>; however with substantial modulations. These new ordering variants will be reported in a separate publication.

#### 3.3 Magnetic properties

Fourteen of the studied samples were pure on the level of X-ray powder diffraction and their temperature dependence of the magnetic susceptibility was studied at a magnetic flux density of 10 kOe (Fig. 4). All samples show weak positive susceptibility values classifying them as Pauli paramagnets (the Pauli contribution over-compensates the intrinsic diamagnetism). The room temperature susceptibility values are listed in Table 8. While some samples (especially ZrCoGa and NbRhGa) show almost temperature independent susceptibility courses, most others show increases in the low-temperature regimes, pointing to minor amounts of paramagnetic impurities. Such paramagnetic phases have some orders of magnitude higher molar susceptibilities and thus already very small amounts (mostly << 1%) strongly affect the Pauli paramagnetism characteristics of the samples. The largest influence is observed for the TaMnGa sample, where the impurity phase is already evident at T = 150 K. Data for the ScNiGa sample are included in Table 8. The susceptibility is higher than that of ScPtGa and ScAuGa, most likely due to paramagnetic nickel at the grain boundaries.

#### 3.4 <sup>57</sup>Fe Mössbauer spectroscopy

Figure 5 shows the <sup>57</sup>Fe Mössbauer spectrum of the TaFeGa sample at room temperature. At first sight one might assume the presence of a single signal; however, this would result in a too large line width parameter. The hexagonal Laves phase TaFeGa contains iron atoms on two crystallographically independent sites, as also observed for the isotypic niobium compound NbFe $_{1.51}$ Ga $_{0.49}$ . We have then reproduced the experimental spectrum with a superposition of two sub-signals: Fe1 with  $\delta = 0.06(3)$  mm s<sup>-1</sup>,  $\Delta E_0 = 0.18(4) \text{ mm s}^{-1}$ ,  $\Gamma = 0.30 \text{ mm s}^{-1}$ , 43% area and Fe2 with  $\delta = -0.02(3) \text{ mm s}^{-1}, \Delta E_0 = 0.26(3) \text{ mm s}^{-1}, \Gamma = 0.32(3) \text{ mm s}^{-1},$ 57% area. The line width parameter of Fe1 was fixed to 0.30 mm s<sup>-1</sup> in order to avoid correlations.

The isomer shift values around 0 mm s<sup>-1</sup> show more or less metallic iron. They compare well with the values recently

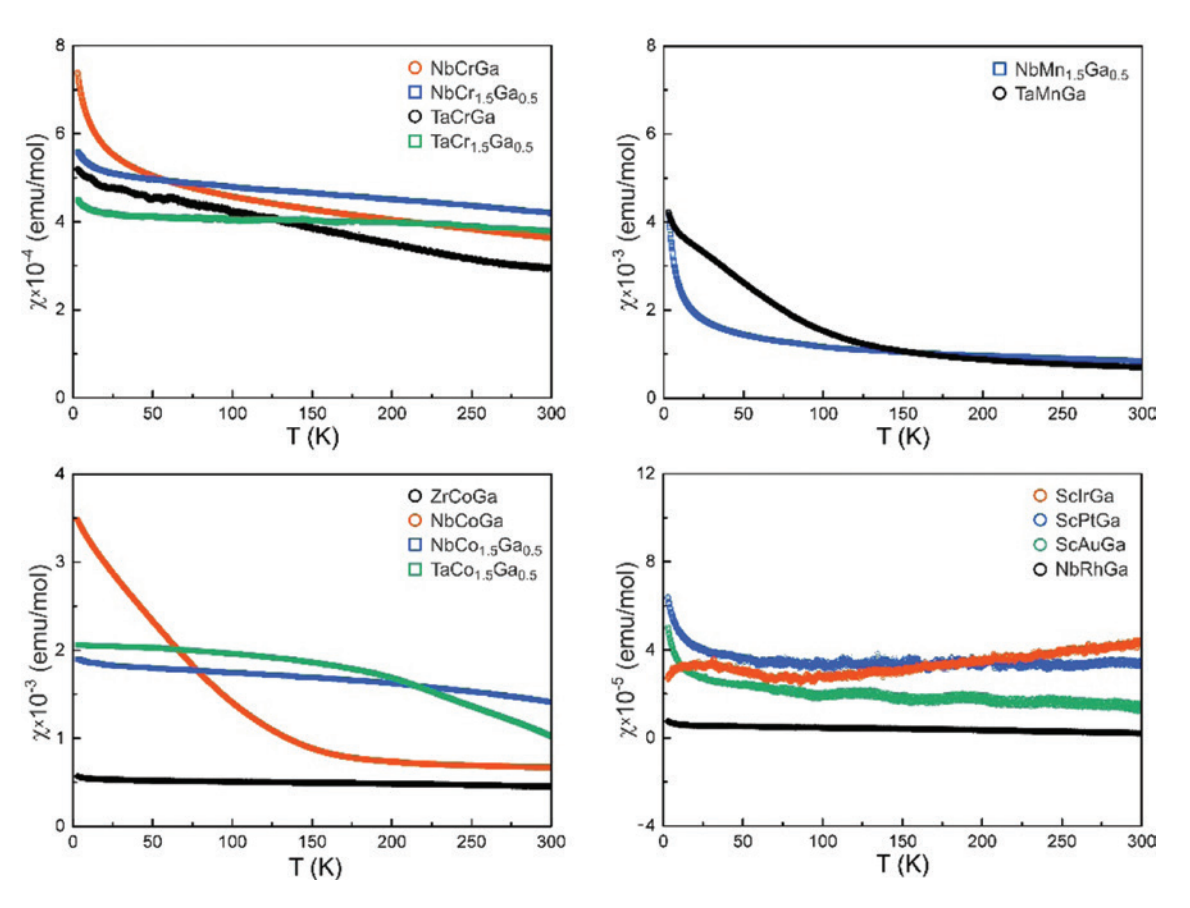


Fig. 4: Temperature dependence of the molar susceptibility of diverse ternary transition metal gallide phases (10 kOe data). The room temperature susceptibilities are summarized in Table 8.

Table 8: Room temperature magnetic susceptibilities measured with a flux density of 10 kOe.

Compound	χ <sub>(300 K)</sub> (emu mol⁻¹)
ScNiGa	1.29(2)×10 <sup>-4</sup>
ScIrGa	$4.2(2) \times 10^{-5}$
ScPtGa	$3.3(2) \times 10^{-5}$
ScAuGa	$1.5(2) \times 10^{-5}$
ZrCoGa	$4.50(2) \times 10^{-4}$
NbCrGa	$7.84(2) \times 10^{-4}$
NbCr <sub>1.5</sub> Ga <sub>0.5</sub>	$4.20(2) \times 10^{-4}$
NbMn <sub>1.5</sub> Ga <sub>0.5</sub>	$8.45(2) \times 10^{-4}$
NbCoGa	$6.68(2) \times 10^{-4}$
NbCo <sub>1.5</sub> Ga <sub>0.5</sub>	$1.41(1) \times 10^{-3}$
NbRhGa	$2.1(5) \times 10^{-6}$
TaMnGa	$7.03(2) \times 10^{-4}$
TaCrGa	$2.94(2) \times 10^{-4}$
TaCr <sub>1.5</sub> Ga <sub>0.5</sub>	$3.79(2) \times 10^{-4}$
TaCo <sub>1.5</sub> Ga <sub>0.5</sub>	$1.02(1) \times 10^{-3}$

determined for the series of TFeSi and TFeGe (T=Zr, Nb, Hf, Ta) tetrelides [55]. Keeping the areas of the two sub-signals in mind, we can assume occupancies of approximately 86%

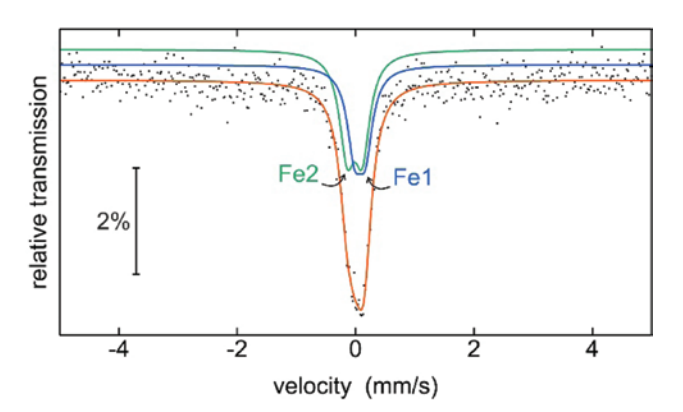


Fig. 5: Experimental and simulated <sup>57</sup>Fe Mössbauer spectrum of the TaFeGa sample. The subspectra of the two crystallographically independent iron sites are emphasized (blue and green subspectra) and the simulated complete spectrum is drawn in red.

Fe1/14% Ga1 for the 2a and 38% Fe2/62% Ga2 for the 6h site of our TaFeGe sample. The quadrupole splitting parameters reflect non-cubic site symmetries,  $\overline{3}m$ . for Fe1 and mm2 for Fe2. The lower site symmetry of Fe2 leads to the slightly higher  $\Delta E_0$  value of 0.26(3) mm s<sup>-1</sup>.

Acknowledgements: We thank Dr. Rolf-Dieter Hoffmann and Dipl.-Ing. Jutta Kösters for collecting the single-crystal intensity data.

#### References

- [1] R. Ferro, A. Saccone, Intermetallic Chemistry, Elsevier, Amsterdam. 2008.
- [2] R. Pöttgen, D. Johrendt, Intermetallics, De Gruyter, Berlin, 2014.
- [3] W. Steurer, J. Dshemuchadse, Intermetallics: Structures, Properties, and Statistics, IUCr Monographs on Crystallography, Vol. 26, Oxford University Press, New York, 2016. ISBN-10: 0198714556.
- [4] P. Villars, K. Cenzual, Pearson's Crystal Data: Crystal Structure Database for Inorganic Compounds (release 2018/19), ASM International®, Materials Park, Ohio (USA) 2018.
- [5] R. L. Johnston, R. Hoffmann, Z. Anorg. Allg. Chem. 1992, 616, 105.
- [6] R. Nesper, G. J. Miller, J. Alloys Compd. 1993, 197, 109.
- [7] A. Von Keitz, G. Sauthoff, Intermetallics 2002, 10, 497.
- [8] S. Amerioun, S. I. Simak, U. Häussermann, Inorg. Chem. 2003, 42, 1467,
- [9] F. Stein, M. Palm, G. Sauthoff, Intermetallics 2004, 12, 713.
- [10] A. Ormeci, A. Simon, Yu. Grin, Angew. Chem. Int. Ed. 2010, 49,
- [11] S. Thimmaiah, G. J. Miller, Z. Anorg. Allg. Chem. 2015, 641, 1486.
- [12] H. Witte, Metallwirtsch. Metallwiss. Metalltech. 1939, 18, 459.
- [13] D. Noréus, L. Eriksson, L. Göthe, P.-E. Werner, J. Less-Common Met. 1985, 107, 345.
- [14] S. Seidel, O. Janka, C. Benndorf, B. Mausolf, F. Haarmann, H. Eckert, L. Heletta, R. Pöttgen, Z. Naturforsch. 2017, 72b, 289.
- [15] O. Osters, T. Nilges, M. Schöneich, P. Schmidt, J. Rothballer, F. Pielnhofer, R. Weihrich, Inorg. Chem. 2012, 51, 8119.
- [16] E. I. Gladyshevskii, P. I. Krypyakevich, M. Y. Teslyuk, Dopov. Akad. Nauk. SSSR 1952, 85, 81.
- [17] K. Osamura, Y. Murakami, J. Less-Common Met. 1978, 60, 311.
- [18] S. Seidel, R. Pöttgen, Z. Anorg. Allg. Chem. 2017, 643, 261.
- [19] F. Eustermann, A. Pominov, R. Pöttgen, Z. Anorg. Allg. Chem. 2018, 644, 1297.
- [20] R. Pöttgen, T. Gulden, A. Simon, GIT Labor-Fachzeitschrift 1999, 43, 133.
- [21] K. Yvon, W. Jeitschko, E. Parthé, J. Appl. Crystallogr. 1977, 10, 73.
- [22] I. S. Gavrilenko, V. Ya. Markiv, Dopov. Akad. Nauk Ukr. RSR, Ser. A 1978, 271.
- [23] I. S. Gavrilenko, V. Ya. Markiv, Metallofizika 1979, 75, 103.
- [24] E. Ganglberger, H. Nowotny, F. Benesovsky, Monatsh. Chem. **1965**, 96, 1658.
- [25] M. Dryś, J. Less-Common Met. 1980, 75, 261.

- [26] M. Yu. Teslyuk, V. Ya. Markiv, E. I. Gladyshevskii, J. Struct. Chem. 1964, 5, 364.
- [27] V. Ya. Markiv, Y. V. Voroshilov, P. I. Krypyakevych, E. E. Cherkashin, Sov. Phys. Crystallogr. 1965, 9, 619.
- [28] E. M. Savitskii, Y. V. Efimov, V. Ya. Markiv, A. I. Storozhenko, O. I. Zvolinskii, Russ. Metall. 1978, 1, 183.
- [29] A. E. Dwight, Proc. Rare Earth Res. Conf. 7th, 1969, 1, 273.
- [30] V. Y. Markiv, N. N. Belyavina, I. S. Gavrilenko, Russ. Metall. **1984**, 5, 227.
- [31] E. Hovestreydt, N. Engel, K. Klepp, B. Chabot, E. Parthé, J. Less-Common Met. 1982, 85, 247.
- [32] G. J. Long, T. E. Cranshaw, G. Longworth, Mössbauer Eff. Ref. Data J. 1983, 6, 42.
- [33] R. A. Brand, WINNORMOS for IGOR6 (Version for IGOR 6.2 or above: 22.02.2017), Universität Duisburg, Duisburg, Germany, 2017.
- [34] L. Palatinus, Acta Crystallogr. B 2013, 69, 1.
- [35] L. Palatinus, G. Chapuis, J. Appl. Crystallogr. 2007, 40, 786.
- [36] V. Petříček, M. Dušek, L. Palatinus, Z. Kristallogr. 2014, 229, 345.
- [37] J. W. Nielsen, N. C. Baenziger, Acta Crystallogr. 1954, 7, 132.
- [38] C. Brink Shoemaker, D. P. Shoemaker, Acta Crystallogr. 1965, 18, 900.
- [39] R.-D. Hoffmann, R. Pöttgen, Z. Kristallogr. 2001, 216, 127.
- [40] R. Pöttgen, Z. Anorg. Allg. Chem. 2014, 640, 869.
- [41] V. B. Compton, Acta Crystallogr. 1958, 11, 446.
- [42] B. H. Verbeek, H. W. A. M. Rompa, P. K. Larsen, M. S. Methfessel, F. M. Mueller, Phys. Rev. B 1983, 28, 6774.
- [43] L. Heletta, S. Seidel, C. Benndorf, H. Eckert, R. Pöttgen, Z. Naturforsch. 2017, 72b, 609.
- [44] F. Hulliger, J. Alloys Compd. 1996, 239, 131.
- [45] J. Emsley, The Elements, Oxford University Press, Oxford, 1999.
- [46] J. Donohue, The Structures of the Elements, Wiley, New York,
- [47] J. L. Jorda, J. Muller, H. F. Braun, C. Susz, J. Less-Common Met. 1987, 134, 99,
- [48] X. Yan, A. Grytsiv, P. Rogl, H. Schmidt, G. Giester, A. Saccone, X.-Q. Chen, Intermetallics 2009, 17, 336.
- [49] R. Pöttgen, W. Jeitschko, Inorg. Chem. 1991, 30, 427.
- [50] T. Harmening, L. van Wüllen, H. Eckert, U. Ch. Rodewald, R. Pöttgen, Z. Anorg. Allg. Chem. 2010, 636, 972.
- [51] L. Heletta, S. F. Matar, R. Pöttgen, Z. Naturforsch. 2019, 74b, 15.
- [52] E. Parthé, L. Gelato, B. Chabot, M. Penzo, K. Cenzual, R. Gladyshevskii, TYPIX-Standardized Data and Crystal Chemical Characterization of Inorganic Structure Types, Gmelin Handbook of Inorganic and Organometallic Chemistry, 8th edition, Springer, Berlin (Germany), 1993.
- [53] G. Nuspl, K. Polborn, J. Evers, G. A. Landrum, R. Hoffmann, Inorg. Chem. 1996, 35, 6922.
- [54] M. D. Bojin, R. Hoffmann, Helv. Chim. Acta 2003, 86, 1683.
- [55] S. Stein, T. Block, S. Klenner, L. Heletta, R. Pöttgen, Z. Naturforsch. 2019, 74b, 211.